Modelling the combined impact of sea level rise, land subsidence, and tropical cyclones in compound flooding of coastal cities

Wu, Guofeng; Liu, Qing; Xu, Hanqing; Wang, Jun

DOI
10.1016/j.ocecoaman.2024.107107

Publication date
2024

Document Version
Final published version

Published in
Ocean and Coastal Management

Citation (APA)
Wu, G., Liu, Q., Xu, H., & Wang, J. (2024). Modelling the combined impact of sea level rise, land subsidence, and tropical cyclones in compound flooding of coastal cities. *Ocean and Coastal Management*, *252*, Article 107107. https://doi.org/10.1016/j.ocecoaman.2024.107107

Ocean and Coastal Management 252 (2024) 107107

Contents lists available at ScienceDirect

Ocean and Coastal Management

journal homepage: www.elsevier.com/locate/ocecoaman

Modelling the combined impact of sea level rise, land subsidence, and tropical cyclones in compound flooding of coastal cities

Guofeng Wu [a,b,c], Qing Liu [a,b,c], Hanqing Xu [a,b,c,d,e,f,**], Jun Wang [a,b,c,*]

[a] Key Laboratory of Geographic Information Science (Ministry of Education), East China Normal University, Shanghai 200241, China
[b] Institute for National Safety and Emergency Management, East China Normal University, Shanghai 200062, China
[c] School of Geographic Science, East China Normal University, Shanghai 200241, China
[d] Institute of Eco-Chongming (IEC), East China Normal University, Shanghai 200241, China
[e] Delft University of Technology, Delft, 2628CN, the Netherlands
[f] Shanghai Key Lab for Urban Ecological Processes and Eco-Restoration, East China Normal University, Shanghai 200241, China

ARTICLE INFO

Keywords:
Climate change
Compound flooding
Relative sea level rise
Hydrodynamic modeling
PS-InSAR

ABSTRACT

Low-lying coastal areas are threatened worldwide by compound flooding effects, including sea-level rise (SLR), frequent tropical cyclones (TCs), and accelerated land subsidence (LS). Compound flooding results in a negative effect, creating challenges for decision-making and coastal management for sustainable urban development. To comprehend the precise consequences and the combined effect of LS and SLR on coastal cities and to inform management scientifically, we initially chose historical TCs (TC6311 and TC1415) that resulted in exceptionally high surges and significant losses as reference scenarios for simulating potential compound events. We then utilized a hydrodynamic model, which combines TCs, LS, and SLR, to simulate the combined impact of flood hazards. Our findings indicated that the highest subsidence rate exceeds −20 mm/yr, the cumulative subsidence reaches −119.09 mm and 68.44% of the land is experiencing subsidence from 2015 to 2021. When comparing flood scenarios with and without the influence of SLR, the most severely affected by LS is projected to become submerged and completely inundated by 2100. We found that the combined impact of SLR and LS significantly amplified flood inundation and SLR is the primary amplification factor of flooding, projected to account for 46.2% by 2100. The framework established in this study facilitates the quantitative assessment of the interactions among multi-driver factors of compound flooding, thereby serving as a supplementary and guiding tool for future risk management.

1. Introduction

Coastal compound flooding resulting from the combined effects of various meteorological, hydrological, and hydrodynamic processes, poses significant challenges to coastal cities (Fang et al., 2021). In particular, compound flooding during tropical cyclones (TCs) leads to extreme flood inundation, causing destructive impacts (Feng et al., 2019; Marsooli and Lin, 2020; Xu et al., 2023). The vulnerability of coastal areas is further exacerbated by relative sea level rise (RSLR), with sea level rise (SLR) amplifying the frequency, extent, and impact of floods (IPCC et al., 2022). Additionally, land subsidence (LS) plays a crucial role in RSLR in coastal regions (Nicholls et al., 2021; Parsons et al., 2023). When TCs coincide with RSLR, the resulting compound flooding becomes increasingly complex and challenging to manage under global warming. Therefore, it is essential to comprehensively consider the interactions between the multi-drivers of compound flooding to scientifically assess potential compound flooding scenarios.

Coastal areas are highly vulnerable due to the interweaving of human activities and the natural environment (Fang et al., 2020; Zhao and Liu, 2020). In China, low-lying coastal areas are inhabited by over 12% of the population but account for only 2% of the national land area (Liu et al., 2013; Fang et al., 2020, 2021). Studies have indicated that global SLR will render the 100-year return period (RP) flood events, currently experienced as rare, to become commonplace by 2100 (Oppenheimer et al., 2019; Garner et al., 2017; Amoura and Dahmani, 2022). Extremely high-water levels not only have the potential to overshoot their banks but can also reduce the drainage capacity of rivers, causing the backwater effect and urban inundation (Hadipour

* Corresponding author. Key Laboratory of Geographic Information Science (Ministry of Education), East China Normal University, Shanghai 200241, China.
** Corresponding author. Key Laboratory of Geographic Information Science (Ministry of Education), East China Normal University, Shanghai 200241, China.
E-mail addresses: 51253901020@stu.ecnu.edu.cn (G. Wu), uniqliu@163.com (Q. Liu), hqxu@chm.ecnu.edu.cn (H. Xu), jwang@geo.ecnu.edu.cn (J. Wang).

https://doi.org/10.1016/j.ocecoaman.2024.107107
Received 6 November 2023; Received in revised form 2 February 2024; Accepted 20 March 2024
Available online 1 April 2024

et al., 2020; Hsiao et al., 2021; Wang and Marsooli, 2021). Hence, effectively simulating and quantifying the combined impacts of multi-drivers is crucial for enhancing our understanding and preparation for future coastal flood risks.

In addition to SLR, LS can also increase flood risk (Wang et al., 2012; Chen et al., 2018; Yin et al., 2020). LS amplifies the consequences of RSLR on coastal flooding, with individuals living in subsiding cities experiencing SLR at a rate four times faster than that of stable regions globally (Nicholls et al., 2021; Zhao et al., 2021; Fang et al., 2022). Considering regional average LS rates or assumed targets are inadequate for managing localized coastal flooding. Consequently, the incorporation of Permanent Scatterers Synthetic Aperture Radar Interferometry (PS-InSAR) technology in LS monitoring has provided exceptional precision (Ramirez et al., 2022). Some studies have combined PS-InSARmonitored LS with SLR to assess RSLR and flood inundation risk (Catalao et al., 2020; Gao et al., 2021). The combination of localized sea-level variations and refined LS helps identify critical height-vulnerable areas, enabling better support for adaptive strategies and decision-making.

Traditional flood risk assessment methods often consider flood drivers independently (Gao et al., 2023). However, compound flooding caused by multi-drivers often amplifies the harm (Wahl et al., 2015; Bevacqua et al., 2019; Santiago-Collazo et al., 2019). The compound flood risk cannot be simply calculated as the linear sum of risks from individual drivers (Xu et al., 2019; Liu et al., 2022). Recent research primarily focuses on precipitation and storm surge as two driver factors in compound floods (Xu et al., 2022; Eilander et al., 2023). Statistical models and dynamic numerical models are the main methods used to study compound flood risk. For example, Xu et al. (2023) evaluated the dependence relationship of heavy precipitation coinciding with high storm surges in 26 coastal basins in China using a Copula model. Gori et al. (2020a) employed a hydrological model to demonstrate that these two factors often overlap and interact in time and space, thereby increasing the compound risk in coastal areas.

In this study, we developed a comprehensive compound flood hazard assessment framework using Haikou as an example, which integrates TCs, SLR, and LS. The quantitatively analyzed framework through the following steps: (1) construct RSLR scenarios based on local SLR and LS data obtained through PS-InSAR technology; (2) select historical events and simulate compound flood disasters under various RSLR scenarios using the Delft3D Flexible Mesh (D-Flow FM) model; (3) explore flood inundation sensitivity and the combined effects of TCs, LS, and SLR using the flood amplification factor (IR); (4) discuss the relative contributions of SLR and LS to the compound effects (Fig. 1). This work aims to provide robust scientific references and supplements for the recalibration and formulation of coastal sustainable planning and risk reduction measures under climate change.

2. Materials

2.1. Study area

Haikou is located in the northeast of Hainan Island, China. It borders the Qiongzhou Strait to the north, with Guangdong Province across the sea (Fig. 2). Haikou has a tropical monsoon maritime climate with an annual average temperature of 24–24.8 °C and annual cumulative rainfall of 1500–2000 mm. Haikou is also frequently affected by TCs, with the peak period from July to October. Typically, TCs originate from the South China Sea or the Pacific Ocean and impact Haikou after traversing Hainan Island.

During TC No. 11 in 1963 (TC6311), the maximum tide level observed at the Haikou tidal gauge ascended to 4.05 m, corresponding to the water level associated with a 50-year RP. During Typhoon Kalmaegi in 2014 (TC1415), the maximum tidal level at Xiuying tidal gauge reached 4.52 m, corresponding to the water level with a 100-year RP, breaking the record since 1948 around Haikou. TC6311 broke 94 seawalls and inundated 51.20 km^2 of cropland, more than 70 thousand houses collapsed and 80 thousand others were damaged. During Typhoon Kalmaegi (2014), the compound flooding led to a direct economic loss of approximately 220 million US dollars (Liu et al., 2022).

Haikou has the LS risk due to the rapidly increasing urbanization rate, rising from 75.48% in 2012 to 82.73% in 2022. Moreover, the 2022 China Sea Level Bulletin[1] shows that the SLR rate at the Haikou Ocean Station is greater than 4 mm/yr (1980–2022), exceeding the global SLR rate. Under climate change, Haikou would encounter increased challenges related to compound flooding risks from the combined effects of SLR and LS in the future.

2.2. Dataset

SAR Data: Synthetic aperture radar (SAR) data is procured from the Sentinel-1A satellite's C-band SAR Instrument in IW mode (https://search.asf.alaska.edu/). The imagery covers the northern part of Hainan Province and the southern part of Guangdong Province. The imagery's spatial resolution is 5 × 20 m, referring to the distance and azimuth.

Precision orbiting ephemeris data (POD): The satellite position and velocity data are obtained through rigorous measurements and orbital motion analysis, which is used to reduce baseline distance errors and make orbit corrections in subsequent data preprocessing (https://s1qc.asf.alaska.edu/aux_poeorb/).

Elevation data: The 2018 Digital Elevation Model (DEM) of Haikou, with a spatial resolution of 5 m, was provided by the Hainan Provincial Department of Emergency Management. Additionally, the dataset incorporates bathymetry insights from the South China Sea and the Gulf of Tonkin, extracted from General Bathymetric Chart of the Oceans (https://www.gebco.net/).

Historical typhoon track dataset: The dataset includes information on the location, central minimum pressure, and maximum wind speeds of TCs in the Northwest Pacific Ocean and South China Sea from 1949 to 2019. The dataset focuses on 66 historical TCs that affected Haikou during this period. Two notable TC events, TC6311 (with a 50-year RP) and TC1415 (with a 100-year RP) were studied and used. For more details on the selection process for these events, refer to Liu et al. (2022).

Historical daily rainfall dataset and flow data: Daily rainfall data from 1960 to 2019 was obtained from the China Meteorological Administration (http://data.cma.cn/). Additionally, we acquired daily flow data from 1960 to 2020 for the Longtang Hydrological Station from the Bureau of Hydrology and Water Resources Survey of Hainan Province.

Regional sea level rise prediction data: SLR predictions for Haikou under three representative concentration paths (RCP2.6, RCP4.5, and RCP8.5) from 2030 to 2200 (based on the year 2000) (Kopp et al., 2014) (see Table 1).

3. Methodology

3.1. PS-InSAR processing for generating land subsidence data

Permanent Scatterers (PS) are solid and stable objects in an area that remain undamaged for years and can continuously transmit and receive signals from SAR satellites. Assuming there are N+1 images, one is chosen as the master image reference, while the rest are referred to as slave images. The initial step in the PS-InSAR algorithm involves generating connectivity maps to establish master-slave relationships for all the images (Fig. S1). Subsequently, all data is aligned to the master image to create interferograms. Then, a de-grading process is employed to eliminate the topographic phase. This is achieved with the assistance of an external DEM and POD, resulting in the generation of k-amplitude

[1] 2022 China Sea Level Bulletin (http://ecs.mnr.gov.cn/gk/gbytj/202306/t20230619_27396.shtml).

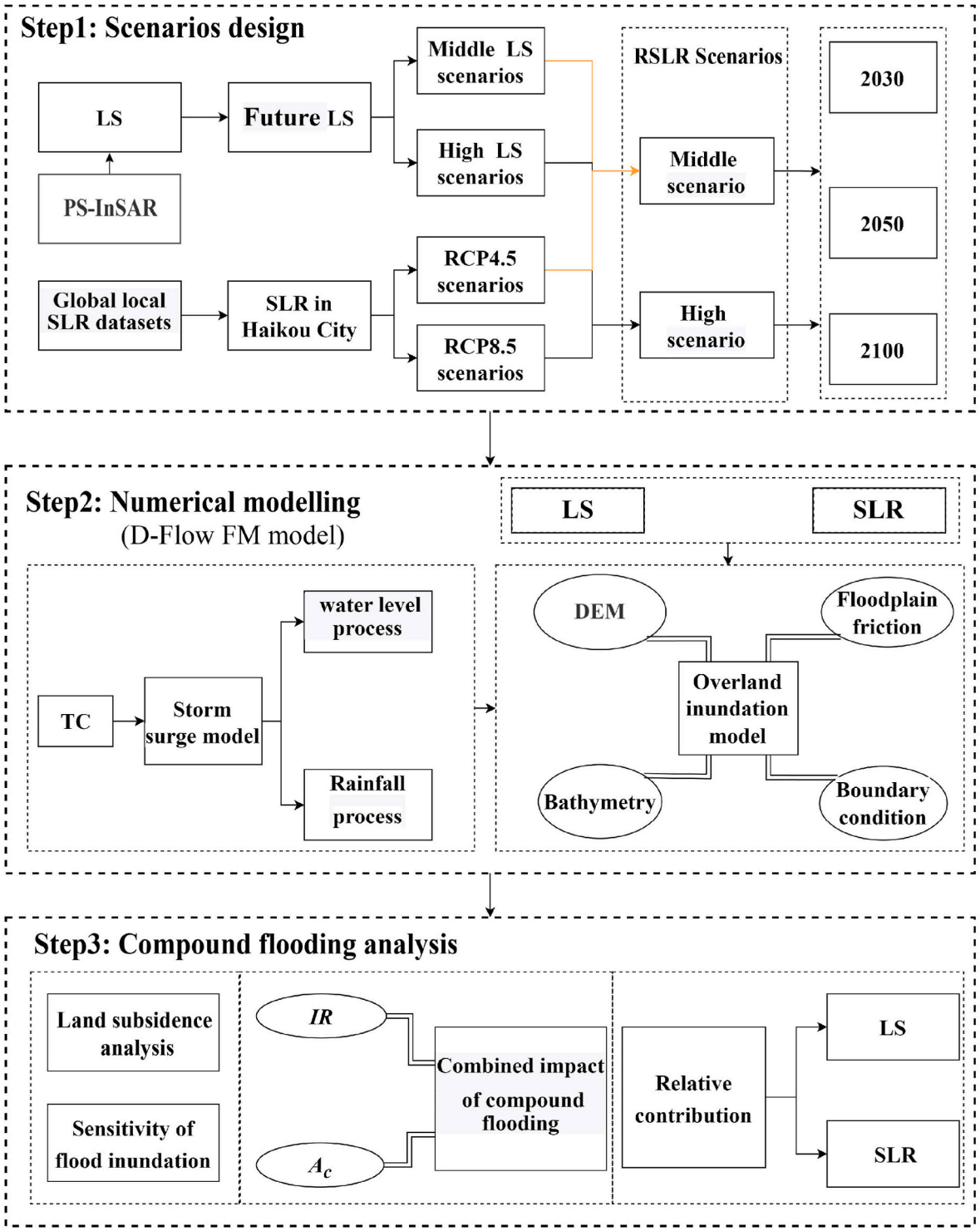

Fig. 1. The flowchart of this study.

differential interferograms. They are screened for persistent scatterers that can maintain high coherence in all interferograms by setting a coherence coefficient threshold. The winding phase at image element point i in the k_{th} interferogram in the differential interferogram can be expressed as (Chen et al., 2022):

$$\varphi_i^k = W\left\{\varphi_{i,def}^k + \varphi_{i,hgt}^k + \varphi_{i,orb}^k + \varphi_{i,atm}^k + \varphi_{i,noise}^k\right\} \quad (1)$$

where $W\{\cdot\}$ is the winding operator, $\varphi_{i,def}^k$ represents the surface deformation phase, $\varphi_{i,hgt}^k$ is the phase associated with elevation errors, $\varphi_{i,orb}^k$ the phase associated with orbital errors, $\varphi_{i,atm}^k$ the atmospheric delay phase, and $\varphi_{i,noise}^k$ is the noise phase.

Temporal and spatial filtering is used to separate the atmospheric delay phase and orbital error phase. Subsequently, the time-series deformation phase and average deformation rate in the direction of the satellite line of sight are determined. The deformation phase reflects the displacement of the ground during the observation time, and the phase change caused by the deformation of the ground point can be

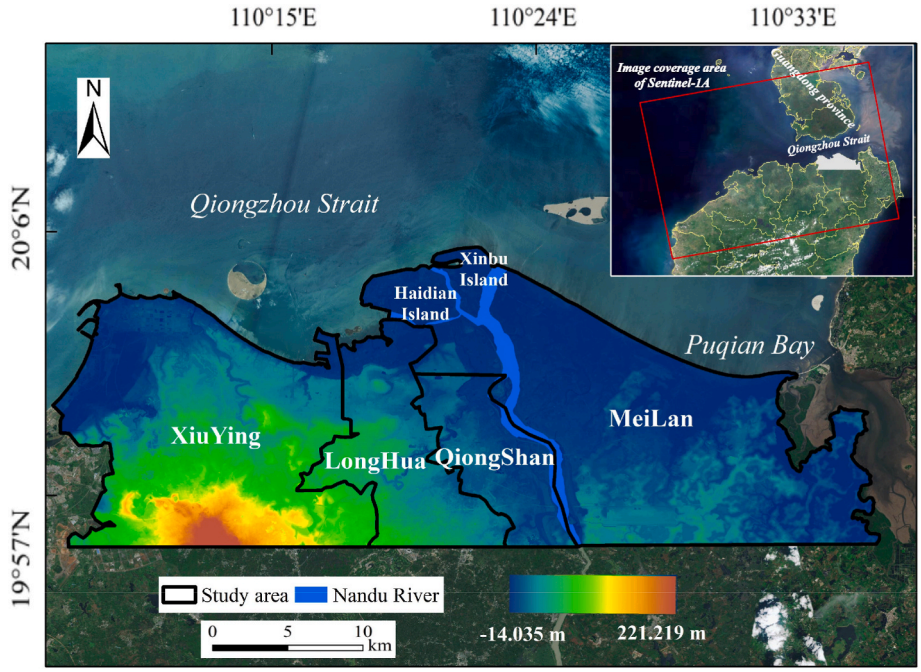

Fig. 2. Geographical location, topography of Haikou City, and image coverage of Sentinel-1A.
The base map is Tianditu, an online mapping service provided by ArcGIS10.8 (http://t0.tianditu.gov.cn/img_c/wmts).

Table 1
Data profile of this study.

Name	Attributes	Source
SAR Data	2015~2021, 5 × 20 m (Table S1)	https://search.asf.alaska.edu/#/ (last accessed: Anytime)
Precision orbiting ephemeris data	Sentinel-1A	https://s1qc.asf.alaska.edu/aux_poeorb/ (last accessed: Anytime)
DEM, Haikou	2018, 5 m	Department of Emergency Management of Hainan Province
DEM, bathymetry	2019, 500 m	https://www.gebco.net/ (last access: December 12, 2019)
TC tracks	1949~2019, 3 hourly	Shanghai Typhoon Research Institute of the China Meteorological Administration
Rainfall dataset	1960~2019, daily	http://data.cma.cn/ (last access: July 16, 2020)
Discharge	1960~2020, daily	Hainan Hydrology and Water Resources Survey Bureau
Regional sea level rise prediction data	2030~2200 (based on the year 2000), the Haikou station	Kopp et al. (2014)

expressed as follows:

$$\varphi_{i,def}^{k} = -\frac{4\pi}{\lambda} d_{LOS} \tag{2}$$

Where λ represents the wavelength of the radar signal, d_{LOS} is the value of LS in the radar line-of-sight direction. The LS in the vertical direction is obtained as follows (Tang et al., 2022):

$$d_{vert} \simeq \frac{d_{LOS}}{\cos_{\theta}} \tag{3}$$

3.2. Future land subsidence scenarios

Based on the historical data collected through the PS-InSAR, we selected the minimum values, representing the maximum subsidence, from the time series of subsidence to be the worst-case scenario for LS. Additionally, the average values represented the middle scenario for the LS. Assuming that the current LS rates from 2015 to 2021 remain constant in the future, this resulted in six potential LS scenarios, 2 for each of the years 2030, 2050, and 2100 (Fig. S2).

Histogram statistics of the LS were analyzed using the middle and high LS scenarios in 2100 (Fig. 3). The distribution under both scenarios was generally similar, indicating that the LS was widespread and relatively consistent. However, the peak position under the middle scenario was at −8.5 mm, with an average cumulative LS of −34.10 mm. On the other hand, the peak position under the high scenario is at −15.5 mm, with an average cumulative LS of −42.57 mm. This suggests that the LS was greater in the high scenario, with a higher number of LS points experienced compared to the middle scenario. Based on the normal distribution's fitted line, the high scenario showed a slight leftward skew compared to the medium scenario.

3.3. Sea level rise projections

The difference between global sea level change and local sea level change is significant. Kopp et al. (2014) conducted a study to project future SLR at different tidal sites worldwide, taking into account melting ice sheets, melting glaciers, oceanic processes, terrestrial water storage, and non-climatic localization as key factors influencing SLR (Kopp et al., 2014). Their projections indicate that, under the RCP8.5 scenario, the sea level change value at the 50th percentile in Haikou is expected to increase from 0.18 m to 0.96 m (relative to the year 2000) between 2030 and 2100. To maintain consistency with the LS scenarios, the SLR projections of Haikou Station from Kopp et al. (2014) were converted to the future change values based on 2015 (Fig. S3). The SLR rate in the sea area from 1993 to 2015 is found to be 5.1 mm/yr, as reported in the 2015 China Sea Level Bulletin.[2] Therefore, we determined that the median SLR of Haikou were 0.1035 m, 0.2535 m, and 0.6735 m for the years 2030, 2050, and 2100 under the RCP4.5 scenario, respectively. For the RCP8.5 scenario, the projected median SLR in the near to medium-term and long-term future for the same timeframes were

[2] 2015 China Sea Level Bulletin (http://gc.mnr.gov.cn/201806/t20180619_1798296.html).

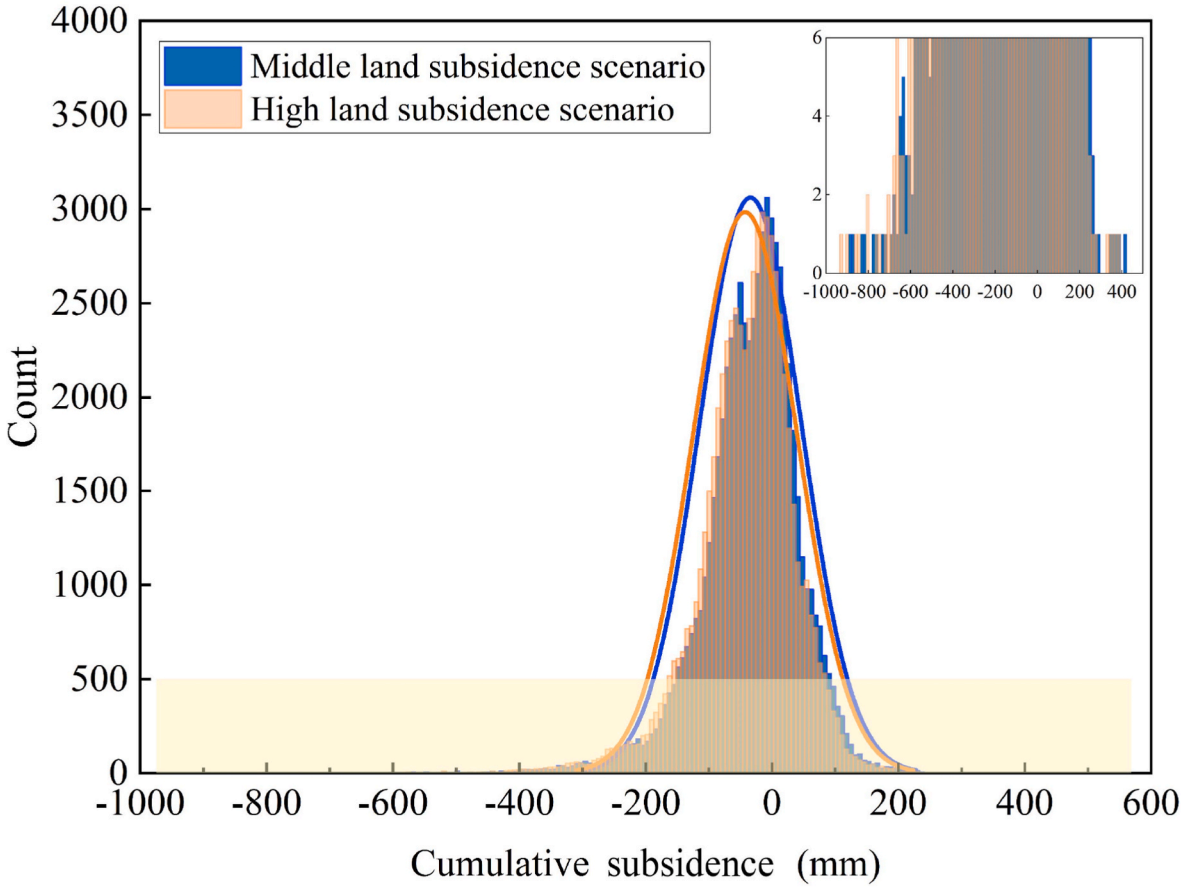

Fig. 3. Histogram statistics of PS points under future middle and high LS scenarios.

0.1035 m, 0.2835 m, and 0.8835 m, respectively (Table 2).

3.4. Flood scenarios and hydrodynamic overland inundation model

To analyze the potential combined impact of LS and SLR on flooding during TCs, we combined the middle LS scenario with the SLR under the RCP4.5 scenario to create the middle RSLR scenarios. Similarly, the high RSLR scenario was created by combining the high LS scenario with the SLR under the RCP8.5 scenario. The 50-year RP compound flood and 100-year RP flood during TCs were combined with different RSLR scenarios, designing 12 combination future flood scenarios (Table 3).

The D-Flow FM model developed by Deltares, Netherlands, has been widely used in the numerical simulation of ocean hydrodynamics and surface runoff (Deltares, 2019). In this study, the D-Flow FM model was employed to develop a compound flood simulation model for Haikou, which encompassed both a storm surge model and an overland inundation model. The storm surge model was capable of estimating coastal tidal levels for each RP. To simulate rainfall and storm surge compound flood events, both coastal tidal levels and extreme rainfall process curves were introduced using the overland inundation model. The upstream boundary condition was set as the average annual discharge at Longtang hydrological station, which was calculated to be 165.81 m^3/s. Both models were validated, and the D-Flow FM model constructed for Haikou is presented in Liu et al. (2022).

We modified the coastal boundary conditions and topographic heights of the model to simulate potential inundation for flood events by different RSLR scenarios (Chen et al., 2018). Subsequently, we elevated the regional sea level change values and modified the storm surge sequence along the coastal boundary.

Table 2
Estimated future sea level rise in Haikou based on 2015.

	RCP4.5 (m)	RCP8.5 (m)
2030	0.1035	0.1035
2050	0.2535	0.2835
2100	0.6735	0.8835

Table 3
Two baseline references and 12 combination future RSLR scenarios.

Return Period	Baseline	RSLR Scenarios		
		2030	2050	2100
50a	B50	S50_2030_mid	S50_2050_mid	S50_2100_mid
		S50_2030_high	S50_2050_high	S50_2100_high
100a	B100	S100_2030_mid	S100_2050_mid	S100_2100_mid
		S100_2030_high	S100_2050_high	S100_2100_high

3.5. Characterization of compound flooding events

To quantify the combined effect of RSLR on floods, additional floodplains were defined as areas where inundation depth increased by more than 0.2 m compared to the baseline reference (A_c) (Gori et al., 2020b). Then, the proportion of A_c area to the original total inundated area under the baseline was calculated as the *IR* to the flood area significantly affected by RSLR. This can be expressed by the following equation:

$$IR = \frac{S_{A_C}}{S_B} \times 100\% \quad (4)$$

Where *IR* represents the increased ratio of flood area affected by RSLR in

%, also known as the inundation amplification factor, S_{A_C} is the additional floodplain area in km,^{2} S_B is the area of flood inundation under normal hydrologic conditions (Baseline) in km.^{2}

4. Results

4.1. LS and accuracy verification

The LS rate map presented 358145 PS points and the results were processed based on the PS-InSAR technique during the period from 2015 to 2021 (Fig. 4). The LS rate ranged from −20.98 to 5.75 mm/yr, and the average value was −0.16 mm/yr with a standard deviation of 1.59 mm/yr. In southern Haidian Island, significant subsidence occurred in Region A, especially on the left bank of the Nandu River, where the maximum rate reached −20.98 mm/yr, approximately 131 times higher than the average LS rate in the entire region. Since Region A was close to the Nandu River and near the estuary, and the terrain was flat, it was susceptible to flooding. A more pronounced crescent-shaped subsidence funnel was observed in Region B, featuring a maximum LS rate of −20.01 mm/yr. It extended across both sides of Nanhai Avenue in Xiuying District. However, Region B's distance from rivers and oceans resulted in a lesser impact of compound flooding compared to Region A.

Cumulative LS was calculated for each period using July 19, 2015, as the reference datum (Fig. S4). The results showed that the north and northeast coastal areas are experiencing LS and the west and northwest coastal areas are experiencing land uplift. As of September 9, 2021, the cumulative maximum subsidence was −119.09 mm and the overall subsidence area increased from 352.13 km^2 to 408.17 km^2, accounting for 68.44%. The average cumulative LS in Region A was −16.74 mm, with the maximum value reaching −119.09 mm, which is approximately 7 times higher than the average cumulative LS. Regions A and B experienced a period of significant subsidence after January 9, 2017, and the area and gradient in the LS center had a clear trend of growth. In 2020, the area formed a clear subsidence funnel and continued to experience subsidence. Meanwhile, the upper reaches of the Nandu River showed obvious patchy and scattered subsidence points along the river direction after 2020.

To verify the reliability of PS-InSAR technology, a 100-m buffer zone centered around leveling points HNHK and Qb3 was created (Yuan et al., 2020). Our average LS rate within this zone was compared to the leveling points. Results indicated a small difference between the PS-InSAR results at HNHK (−0.03 mm/yr, difference of 2.73 mm/yr) and Qb3 (−0.11 mm/yr, difference of 2.61 mm/yr) stations, both within 3 mm/yr. This suggests high accuracy in the monitoring results (Table S2). Furthermore, a comparison with the PS-InSAR monitoring results by Yuan et al. (2020) showed a difference of less than 6 mm at the two leveling points from November 16, 2015, to January 9, 2017 (Fig. S5).

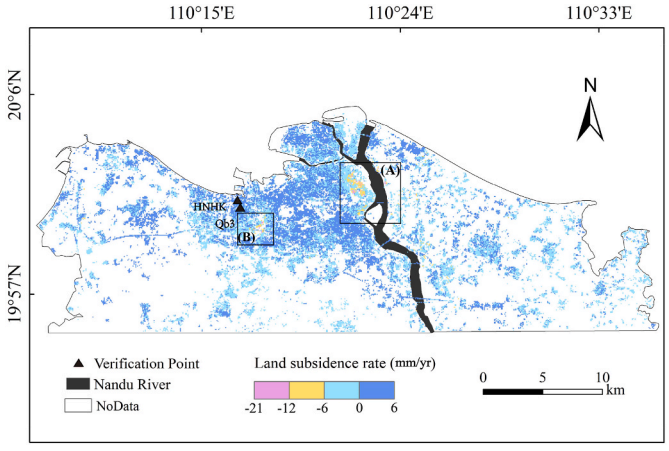

Fig. 4. LS rate between 2015 and 2021 was estimated by PS-InSAR. (Negative rates are referred to as land subsidence. Positive rates mean the land uplift.)

4.2. Sensitivity of inundation to RSLR

Under historical hydrological conditions, the inundation was mainly concentrated in the coastal plain and inland low-lying areas (Fig. S6). The inundation area of the 50-year RP event was 97.23 km^2, accounting for 15.60% of the land area. The inundated area of the 100-year RP event was 106.46 km^2, accounting for about 17.85% of the land area (Table S3). Fig. 5 displays the simulation results for the 12 combined scenarios with RSLR from Table 3. Over time, the inundation extent increased, eventually reaching its peak by 2100. The 100-year RP flood inundation was greater than the 50-year RP flood, and the inundation in the middle RSLR scenario was less than in the high RSLR scenario. To be more specific, the inundation of the 50-year and 100-year RP flood reached 132.70 km^2 and 137.36 km^2 under the middle RSLR scenario in 2100, accounting for about 22.25% and 23.03% of the land area, respectively. The severity was higher under the high RSLR scenario, and the inundation of 140.83 km^2 and 145.49 km^2 accounted for about 23.61% and 24.39% of the land area, respectively.

The RSLR contributed further to an overall increase in the depth and extent of the flood inundation, as observed in multiple combined scenarios, with estuarine coasts being more sensitive to the combined effects (Fig. 6). The inundation area higher than 2 m on Xinbu Island, Jiangdong New District (northeast coast of Melan District), and Haidian Island expanded significantly, and water levels rose along coastlines and river banks under the RSLR scenarios. Additionally, LS amplifies RSLR, and regions experiencing higher LS compared to SLR are most sensitive to compound flooding. In particular, the estuary on the left bank of the Nandu River is highly vulnerable. It will be completely submerged by 2100.

Fig. 7 illustrates the comparison of RSLR effects on inundation depth using the cumulative frequency function. The results demonstrated that higher values deviate from the mean and extend to the right. The right tail extension represents the cumulative probability of extreme events with greater inundation depth. Comparing the inundation depth cumulative curves for different RP flood events under the same RSLR scenario, the overall inundation depth for a 100-year RP flood was greater than that of a 50-year RP at any future point. For flood events with the same RP under the same RSLR scenario, the curve exhibited a gradual rightward shift over time, accompanied by an increase in depth, particularly notable by 2100. In 2030 and 2050, the distribution of inundation depths changes least between the middle and high RSLR scenarios. However, the depth curve for the high scenario in 2100 shifted to the right of the curve for the medium scenario, due to the influence of the extreme RSLR. The aforementioned findings are hence pivotal in enhancing our comprehension of strategic planning for high-risk regions and fostering resilient coastal development for long-term sustainability.

4.3. Compound flood characterization

The *IR* values show the impact of RSLR on compound flooding. Compared to the baseline, the *IR* was 3.56% and 4.03% for the middle and high scenarios in 2030, 12.68% and 14.96% in 2050, and 34.31% and 42.83% in 2100, for a 50-year RP event. The *IR* increased non-uniformly over time, with the most significant impact observed in 2100. The 100-year RP flood had an *IR* equal to 27.65% by 2100 in the middle RSLR scenario but reached 35.16% in the high RSLR scenario. Therefore, the combined effect was more vividly reflected in the high scenario. Additionally, a 50-year RP flood exhibited a higher *IR* compared to a 100-year RP flood under the same RSLR scenarios. Specifically, the *IR* of S50_2100_high was greater than the *IR* of S100_2100_high, the *IR* of S100_2100_high was greater than the *IR* of S50_2100_mid, and the *IR* of the S100_2100_mid scenario was the lowest

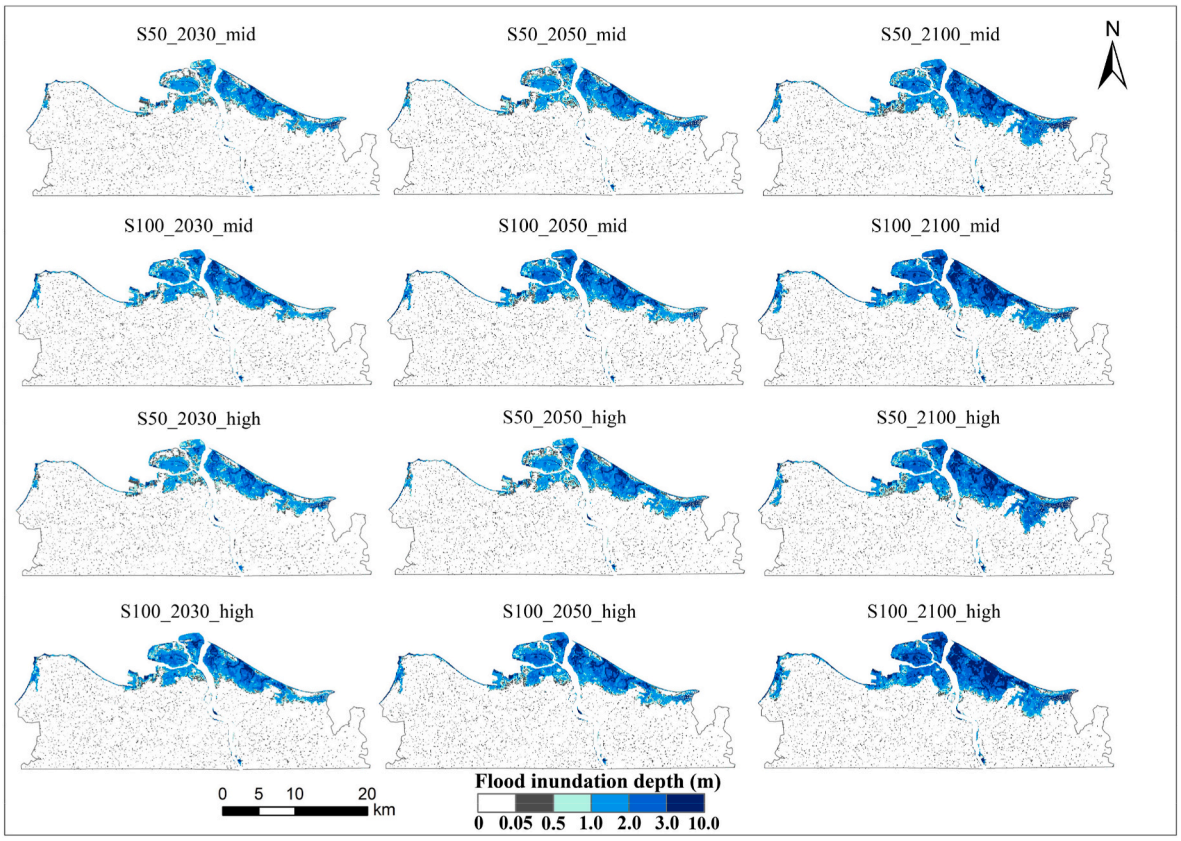

Fig. 5. Flood inundation map for 12 future combined scenarios. The prediction of potential flood hazards by the combined LS and SLR scenarios.

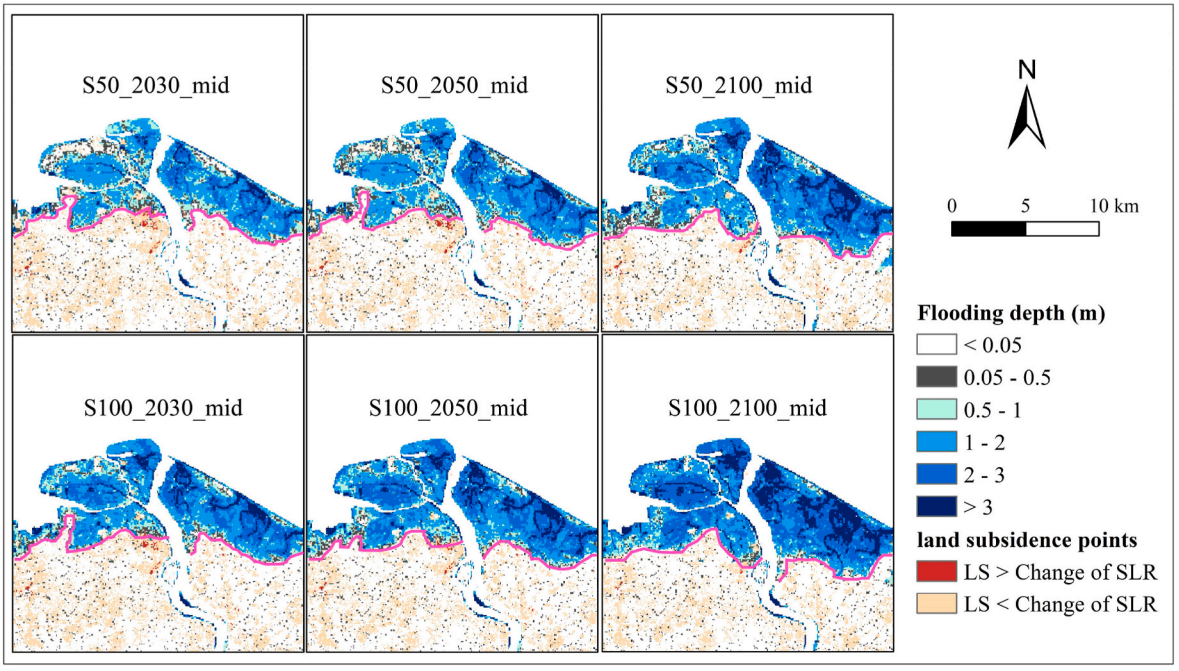

Fig. 6. The flood inundation extent in different return periods under the middle RSLR scenarios. The bottom map shows the LS points. Land uplift is not considered.

(Fig. 8).

Furthermore, the A_c's maximum depth difference for 50-year RP floods in 2030 is 0.44 m and 0.24 m in 2100 in the two RSLR scenarios, while the difference for 100-year RP floods is 0.01 m and 0.32 m, respectively. This suggests that 50-year RP floods were more affected by the RSLR in the short term than 100-year RP floods, but the overall inundation level of 100-year floods will reach the peak in 2100.

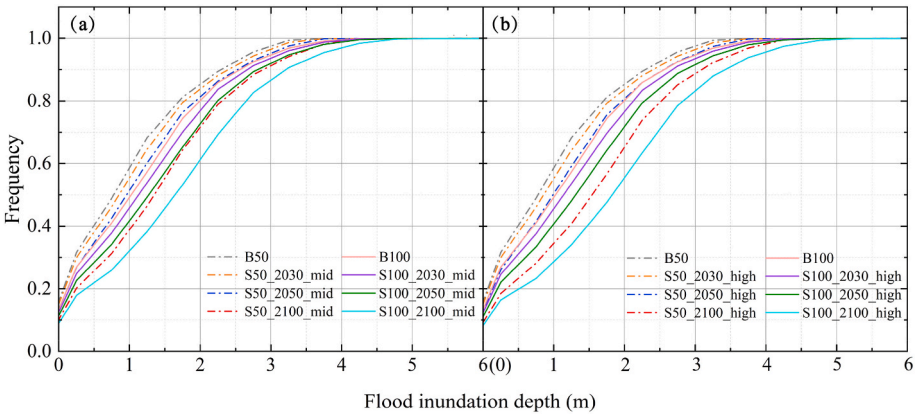

Fig. 7. Cumulative frequency distribution of flood inundation depth in different combined scenarios. The horizontal axis indicates the depth of inundation (m) with a range setting from 0 to 6 m, while the vertical axis indicates the cumulative frequency with a size between 0 and 1.

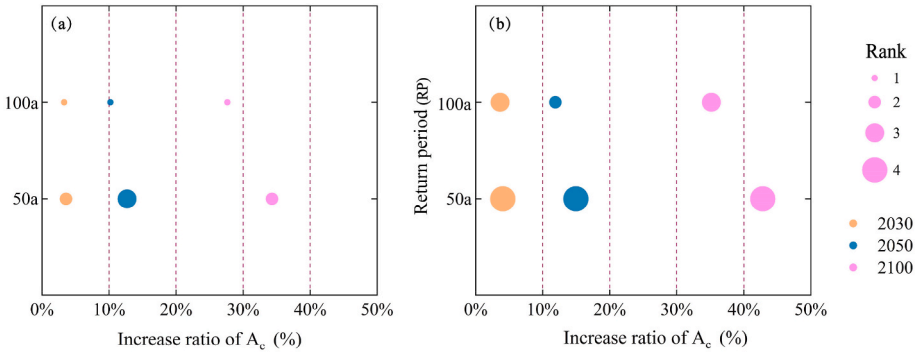

Fig. 8. The *IR* of the inundation area in the middle and high RSLR scenarios. (a) the middle RSLR scenario, and (b) the high RSLR scenario.

5. Discussion

5.1. Combined effects of land subsidence and sea level rise

In this section, we discuss the relative contributions of LS and SLR to the combined impact of compound flooding, which may play a crucial role in enhancing management for coastal areas. To demonstrate that LS and SLR together result in a non-linear impact and obtain the relative contribution of each factor, we conducted separate simulations for compound flood scenarios: (1) SLR alone, (2) LS alone, and (3) RSLR (SLR and LS combined). Fig. 9 illustrates that the inundation area in the RSLR scenario does not linearly align with the sum of flooding scenarios considering LS and SLR independently. This deviation reflects a significant additional effect resulting from the combination of compound flooding factors.

From the perspective of relative contributions from LS and SLR, in the S100_2030_high flood scenario, floods influenced by SLR accounted for 46.3% of the overall compound flood inundation, while LS contributed 44.8%. The contribution of SLR was slightly higher than that of LS by 1.5%. In the S100_2100_high flood scenario, SLR contributed 46.2%,

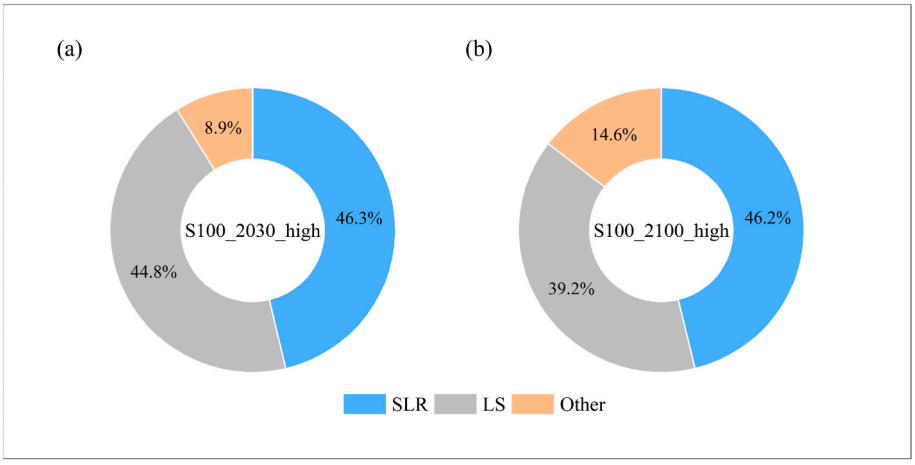

Fig. 9. Relative separate flood contributions from SLR and LS. (a) A 100-year RP flood under the high RSLR scenario by 2030 (S100_2030_high). (b) A 100-year RP flood under the high RSLR scenario by 2100 (S100_2100_high).

while LS contributed 39.2%. In the period from 2030 to 2100, the impact of SLR on compound flooding in Haikou remained relatively stable, but the contribution of LS declined by 5.6%. Considering the additional combined effects, in 2030, under the same flood scenario, the additional contribution of SLR and LS factors in Haikou accounted for an additional 8.9%. By 2100, this additional contribution would increase to 14.6%. From 2030 to 2100, the additional contribution of SLR and LS increased by 5.7%. These results indicate that the interactions between TCs, LS, and SLR would significantly amplify the risks of compound flooding over time.

Consistent with the findings of Wang et al. (2018), both SLR and LS significantly amplify the consequences of flooding, highlighting the primary risks that need to be addressed in coastal compound flooding prevention and management. In the case of Haikou, the long-term risk of SLR outweighs that of LS by 2100, whereas their research suggests that LS poses the greatest risk for Shanghai by 2050. Nevertheless, adaptation to SLR is equally important as subsidence control in coastal areas (Fang et al., 2022). Therefore, upgrading coastal management to integrate SLR adaptation and subsidence control is crucial for enhancing the sustainability of coastal management practices.

5.2. Compound flooding effect and adaptation strategies on the coastal region

The islands of Xinbu and Jiangdong New District suffered the most severe flooding, followed by Haidian Island and the northern part of Longhua District (the main urban area). Our findings are consistent with the study conducted by Zeng et al. (2022). The elevation of Xinbu Island ranges from 1.2 to 3.2 m, with slightly higher elevations at the center of Haidian Island (from 4 to 6 m) and lower elevations at the periphery (from 1 to 3.5 m). Our results indicate that by 2100, the maximum RSLR for Xinbu Island will reach 1.26 m, with a maximum compound flood depth of 5.37 m, nearly submerging the entire island. Haidian Island will experience a maximum RSLR of 1.27 m and a maximum compound flood depth of 5.48 m. However, the current seawall standards in Haikou only protect against a 50-year RP flood event, with a maximum height of approximately 3.5 m. Therefore, the current standards need to be improved. By 2050, the seawall should be raised to 4 m, and for sustainable development and to cope with the compound flooding in 2100, a seawall height of 5.5 m is required.

In coastal areas, storm surges are the primary driver factors, while heavy rainfall is the main factor in inland areas. Lian et al. (2017) suggested that for areas primarily affected by rainfall, reservoir engineering is more effective than pumping station engineering. However, under high tide conditions, pumping station engineering is a more cost-effective choice due to the influence of tidal and flat terrain. In addressing the issue of compound flooding in Haikou, it is recommended to prioritize drainage facilities for the primary driver factors and complement them with other preventive measures. Consideration should be given to low-impact green infrastructure, such as low-lying green spaces, green roofs, and permeable pavements (Liang and Wang, 2019). With climate change, protective infrastructure will face more frequent and costly tests (Johnson, 2023; Rocha et al., 2023). Our results also suggest an urgent need for sea level rise adaptation in the region. Therefore, coastal wetland restoration and wetland landscape construction should be implemented to compensate for the limitations of traditional fixed flood control facilities in effectively addressing SLR (Timmerman et al., 2021).

Simultaneously, a carefully planned retreat strategy should be implemented for Xinbu Island (Mitchell et al., 2020; Klein et al., 2001). Threatened buildings and infrastructure should be relocated to safer areas, with provisions for resettlement and reserved space. It is worth noting that the area on the left side of the Nandu Estuary in the south of Haidian Island experiences obvious LS, it would be completely submerged by 2100, with a projected RSLR of 2.36 m. Due to its proximity to the main urban area attention should be paid to this area. Measures such as land-use planning and policies prohibiting groundwater extraction should be implemented.

Currently, the integration of multiple driving factors of compound floods into coastal management and policies is still limited (Gussmann and Hinkel, 2021). In terms of recommendations for policymakers and decision-makers, our study suggests that addressing compound floods caused by multiple driving factors requires unified management standards and enhanced collaboration. Specific measures include incorporating multi-drivers and combined impacts into urban planning and infrastructure design, integrating both SLR adaptation and LS control, increasing public awareness and participation in risk management, and investing in research and development of innovative adaptation strategies.

6. Conclusions

In this study, we proposed a framework that uses the D-Flow FM model combining SLR, LS, and TCs for quantitative assessment of compound flood hazards in coastal cities. Although this study was limited to Haikou, the methodology of quantitatively assessing compound flooding risks through a hydrodynamic model can be used for other coastal cities.

(1) The LS rate in Haikou ranged from −20.98 to 5.75 mm/yr, with an average LS rate of −0.16 mm/yr and a standard deviation of 1.59 mm/yr from 2015 to 2021. The most serious subsidence funnel appeared on the left bank of the Nandu River in the south of Haidian Island. The maximum LS rate in this area reached −20.98 mm/yr, which was about 131 times the average LS rate in the whole region. Between 2015 and 2021, the average cumulative LS in this area reached −16.74 mm in this subsidence funnel, while the maximum cumulative LS reached −119.09 mm, which was about 7 times the average cumulative LS.

(2) The combination of LS and SLR would amplify flood risk under climate change. In the middle and high RSLR scenarios, the inundated area for the 50-year RP flood was 132.70 km^2 and 140.83 km^2 in 2100, which increased by 5.98% and 7.34% compared with the baseline scenario. This highlights the potential for lower RP floods to escalate into larger-scale disasters. In contrast, the 100-year RP flood, with its larger scale, exhibited a greater increase in magnitude when influenced by RSLR resulting in inundated areas of 137.36 km^2 and 145.49 km^2. Notably, regions with higher LS experienced a more significant impact of RSLR, exemplified by the estuary on the left bank of the Nandu River.

(3) The combined impact of SLR and LS on compound flooding during TCs was not a simple linear addition of individual flood effects. It exceeded the sum of their separate impacts in this study. Furthermore, the combined contribution of SLR and LS grew significantly over time. Within this dynamic, the SLR played a central role in amplifying floods, with the SLR's expected contribution reaching 46.2% by 2100.

(4) The current seawall standards in Haikou are insufficient to address future risks, necessitating improvements and raising the seawall height. LS control and addressing are crucial in the planning and renovation of the Nandu River area. Policies and regulations should be implemented to prohibit groundwater extraction and avoid exacerbating LS. Furthermore, unified management standards and enhanced collaboration among various departments are necessary to effectively deal with compound floods caused by multi-drivers.

Funding information

This work is sponsored by the National Natural Science Foundation of China, China (Grant No. 42371088), the China Postdoctoral Science Foundation, China (Grant No. 2023M731091), the Postdoctoral

Fellowship Program of CPSF, China (Grant No. GZB20230217), and the Shanghai Key Lab for Urban Ecological Processes and Eco-Restoration, China (Grant No. SHUES2023B02).

CRediT authorship contribution statement

Guofeng Wu: Writing – review & editing, Writing – original draft, Visualization, Validation, Software, Methodology, Investigation, Formal analysis, Data curation, Conceptualization. **Qing Liu:** Writing – review & editing, Validation, Software, Methodology, Investigation, Conceptualization. **Hanqing Xu:** Writing – review & editing, Supervision, Methodology, Conceptualization. **Jun Wang:** Writing – review & editing, Supervision, Methodology, Conceptualization.

Declaration of competing interest

The authors declare the following financial interests/personal relationships which may be considered as potential competing interests: Wu Guofeng reports article publishing charges was provided by National Natural Science Foundation of China. If there are other authors, they declare that they have no known competing financial interests or personal relationships that could have appeared to influence the work reported in this paper.

Data availability

Data will be made available on request.

Acknowledgments

This work is sponsored by the National Natural Science Foundation of China (Grant No. 42371088), the China Postdoctoral Science Foundation (Grant No. 2023M731091), the Postdoctoral Fellowship Program of CPSF (Grant No. GZB20230217), the Shanghai Key Lab for Urban Ecological Processes and Eco-Restoration (Grant No. SHUES2023B02). We express our sincere gratitude to the Department of Emergency Management of Hainan Province and the Hainan Hydrology of Water Resource Survey Bureau for supporting the geographic information of the study area.

Appendix A. Supplementary data

Supplementary data to this article can be found online at https://doi.org/10.1016/j.ocecoaman.2024.107107.

References

Amoura, R., Dahmani, K., 2022. Visualization of the spatial extent of flooding expected in the coastal area of Algiers due to sea level rise. Horizon 2030/2100. Ocean Coast Manag. 219, 106041 https://doi.org/10.1016/j.ocecoaman.2022.106041.

Bevacqua, E., Maraun, D., Vousdoukas, M.I., Voukouvalas, E., Voukouvalas, E., Mentaschi, L., Widmann, M., 2019. Higher probability of compound flooding from precipitation and storm surge in Europe under anthropogenic climate change. Sci. Adv. 5 (9), eaaw5531 https://doi.org/10.1126/sciadv.aaw5531.

Catalao, J., Raju, D., Nico, G., 2020. Insar maps of land subsidence and Sea Level scenarios to quantify the flood inundation risk in coastal cities: the case of Singapore. Rem. Sens. 12 (2), 296. https://doi.org/10.3390/rs12020296.

Chen, C.-N., Tfwala, Samkele, 2018. Impacts of climate change and land subsidence on inundation risk. Water 10 (2), 157. https://doi.org/10.3390/w10020157.

Chen, Y., Liao, M., Wu, J., Li, X., Xiong, F., Liu, S., Feng, Y., Wang, X., 2022. Elastic and Inelastic ground deformation in Shanghai Lingang area Revealed by Sentinel-1, leveling, and groundwater level data. Rem. Sens. 14 (11), 2693. https://doi.org/10.3390/rs14112693.

Deltares, 2019. 1D/2D/3D Modelling suite for integral water solutions. Delft3D Flexible Mesh Suite (RGFGRID). Deltares, version: 5.0.

Eilander, D., Couasnon, A., Leijnse, T., Ikeuchi, H., Yamazaki, D., Muis, S., Dullaart, J., Haag, A., Winsemius, H.C., Ward, P.J., 2023. A globally applicable framework for compound flood hazard modeling. Nat. Hazards Earth Syst. Sci. 23 (2), 823–846. https://doi.org/10.5194/nhess-23-823-2023.

Fang, J.Y., Wahl, T., Fang, J., Sun, X., Kong, F., Liu, M., 2021. Compound flood potential from storm surge and heavy precipitation in coastal China: dependence, drivers, and impacts. Hydrol. Earth Syst. Sci. 25 (8), 4403–4416. https://doi.org/10.5194/hess-25-4403-2021.

Fang, J., Lincke, D., Brown, S., Nicholls, R.J., Wolff, C., Merkens, J.-L., Hinkel, J., Vafeidis, A.T., Shi, P., Liu, M., 2020. Coastal flood risks in China through the 21st century – an application of DIVA. Sci. Total Environ. 704, 135311 https://doi.org/10.1016/j.scitotenv.2019.135311.

Fang, J., Nicholls, R.J., Brown, S., Lincke, D., Hinkel, J., Vafeidis, A.T., Du, S., Zhao, Q., Liu, M., Shi, P., 2022. Benefits of subsidence control for coastal flooding in China. Nat. Commun. 13 (1), 6946. https://doi.org/10.1038/s41467-022-34525-w.

Feng, J., Li, D., Wang, T., Liu, Q., Deng, L., Zhao, L., 2019. Acceleration of the extreme Sea Level rise along the Chinese coast. Earth Space Sci. 6 (10), 1942–1956. https://doi.org/10.1029/2019ea000653.

Gao, G., San, L.H., Zhu, Y., 2021. Flood inundation analysis in Penang island (Malaysia) based on InSAR maps of land subsidence and local Sea Level scenarios. Water 13 (11), 1518. https://doi.org/10.3390/w13111518.

Gao, L., Mei, J., Li, J., Zhang, W., Lai, C., 2023. Effect of intense rainfall and high riverine water level on compound flood hazards in a river-valley city: a case study of Yingde, China. J. Hydrol. 625 (Part B), 130044 https://doi.org/10.1016/j.jhydrol.2023.130044.

Garner, A.J., Mann, M.E., Emanuel, K.A., Kopp, R.E., Lin, N., Alley, R.B., Horton, B.P., DeConto, R.M., Donnelly, J.P., Pollard, D., 2017. Impact of climate change on New York City's coastal flood hazard: increasing flood heights from the preindustrial to 2300 CE. Proc. Natl. Acad. Sci. USA 114 (45), 11861–11866. https://doi.org/10.1073/pnas.1703568114.

Gori, A., Lin, N., Smith, J., 2020a. Assessing compound flooding from Landfalling tropical cyclones on the North Carolina coast. Water Resour. Res. 56 (4), e2019WR026788 https://doi.org/10.1029/2019wr026788.

Gori, A., Lin, N., Xi, D., 2020b. Tropical cyclone compound flood hazard assessment: from Investigating drivers to quantifying extreme water levels. Earth's Future 8 (12), e2020EF001660. https://doi.org/10.1029/2020ef001660.

Gussmann, G., Hinkel, J., 2021. A framework for assessing the potential effectiveness of adaptation policies: coastal risks and sea-level rise in the Maldives. Environ. Sci. Pol. 115, 35–42. https://doi.org/10.1016/j.envsci.2020.09.028.

Hadipour, V., Vafaie, F., Kerle, N., 2020. An indicator-based approach to assess social vulnerability of coastal areas to sea-level rise and flooding: a case study of Bandar Abbas city, Iran. Ocean Coast Manag. 188, 105077 https://doi.org/10.1016/j.ocecoaman.2019.105077.

Hsiao, S.C., Chiang, W.S., Jang, J.H., Wu, H.L., Lu, W.S., Chen, W.B., Wu, Y.T., 2021. Flood risk influenced by the compound effect of storm surge and rainfall under climate change for low-lying coastal areas. Sci. Total Environ. 764, 144439 https://doi.org/10.1016/j.scitotenv.2020.144439.

IPCC, 2022. In: Portner, H.-O., Roberts, D.C., Tignor, M., Poloczanska, E.S., Mintenbeck, K., Alegría, A., Craig, M., Langsdorf, S., Loschke, S., Moller, V., Okem, A., Rama, B. (Eds.), Intergovernmental Panel on Climate Change, Climate Change 2022: Impacts, Adaptation and Vulnerability. Contribution of Working Group II to the Sixth Assessment Report of the Intergovernmental Panel on Climate Change. Cambridge University Press, Cambridge, UK and New York, NY, USA. November 2022. https://www.ipcc.ch/assessment-report/ar6/.

Johnson, D.R., 2023. Defence against the rising seas. Nat. Clim. Change 13 (4), 313–314. https://doi.org/10.1038/s41558-023-01645-0.

Klein, R.J.T., Nicholls, R.J., Ragoonaden, S., Capobianco, M., Aston, J., Buckley, E.N., 2001. Technological options for adaptation to climate change in coastal zones. J. Coast Res. 17 (3), 531–543. https://www.jstor.org/stable/4300206.

Kopp, R.E., Horton, R.M., Little, C.M., Mitrovica, J.X., Oppenheimer, M., Rasmussen, D. J., Strauss, B.H., Tebaldi, C., 2014. Probabilistic 21st and 22nd century sea-level projections at a global network of tide-gauge sites. Earth's Future 2 (8), 383–406. https://doi.org/10.1002/2014ef000239.

Lian, J., Xu, H., Xu, K., Ma, C., 2017. Optimal management of the flooding risk caused by the joint occurrence of extreme rainfall and high tide level in a coastal city. Nat. Hazards 89 (1), 183–200. https://doi.org/10.1007/s11069-017-2958-4.

Liang, M., Wang, H., 2019. Study on the Ecological landscape design of Yawei Creek wetland based on LID. IOP Conf. Ser. Earth Environ. Sci. 330 (2), 022115 https://doi.org/10.1088/1755-1315/330/2/022115.

Liu, J., Wen, J., Huang, Y., Shi, M., Meng, Q., Ding, J., Xu, H., 2013. Human settlement and regional development in the context of climate change: a spatial analysis of low elevation coastal zones in China. Mitig. Adapt. Strategies Glob. Change 20 (4), 527–546. https://doi.org/10.1007/s11027-013-9506-7.

Liu, Q., Xu, H., Wang, J., 2022. Assessing tropical cyclone compound flood risk using hydrodynamic modelling: a case study in Haikou City, China. Nat. Hazards Earth Syst. Sci. 22 (2), 665–675. https://doi.org/10.5194/nhess-22-665-2022.

Marsooli, R., Lin, N., 2020. Impacts of climate change on hurricane flood hazards in Jamaica Bay, New York. Climatic Change 163 (4), 2153–2171. https://doi.org/10.1007/s10584-020-02932-x.

Mitchell, M., Herman, J., Hershner, C., 2020. Evolution of tidal Marsh distribution under accelerating Sea Level rise. Wetlands 40 (6), 1789–1800. https://doi.org/10.1007/s13157-020-01387-1.

Nicholls, R.J., Lincke, D., Hinkel, J., Brown, S., Vafeidis, A.T., Meyssignac, B., Hanson, S. E., Merkens, J.-L., Fang, J., 2021. A global analysis of subsidence, relative sea-level change and coastal flood exposure. Nat. Clim. Change 11 (4), 338–342. https://doi.org/10.1038/s41558-021-00993-z.

Oppenheimer, M., Glavovic, B.C., Hinkel, J., Wal, R., Magnan, A.K., Abd-Eigawad, A.M., Cai, R., Cifuentes-Jara, M., DeConto, R.M., Ghosh, T., Hay, J.E., Isla, F.I., Marzeion, B., Meyssignac, B., Sebesvari, Z., 2019. Sea Level Rise and Implications for Low-Lying Islands, Coasts and Communities. IPCC. https://doi.org/10.1017/9781009157964.006.

Parsons, T., Wu, P.C., Wei, M., D'Hondt, S., 2023. The Weight of New York city: Possible contributions to subsidence from anthropogenic Sources. Earth's Future 11 (5), e2022EF003465. https://doi.org/10.1029/2022ef003465.

Ramirez, Angeles, Kwon, R., Hyuk, Tae, 2022. Sentinel-1 persistent scatterer Interferometric Synthetic aperture radar (PS-InSAR) for long-term Remote monitoring of ground subsidence: a case study of a Port in Busan, South Korea. KSCE J. Civ. Eng. 26 (10), 4317–4329. https://doi.org/10.1007/s12205-022-1005-5.

Rocha, C., Antunes, C., Catita, C., 2023. Coastal indices to assess sea-level rise impacts - a brief review of the last decade. Ocean Coast Manag. 237, 106536 https://doi.org/10.1016/j.ocecoaman.2023.106536.

Santiago-Collazo, F.L., Bilskie, M.V., Hagen, S.C., 2019. A comprehensive review of compound inundation models in low-gradient coastal watersheds. Environ. Model. Software: with environment data news 119, 166–181. https://doi.org/10.1016/j.envsoft.2019.06.002.

Tang, M., Zhao, Q., Pepe, A., Devlin, A.T., Falabella, F., Yao, C., Li, Z., 2022. Changes of Chinese coastal regions Induced by land Reclamation as Revealed through TanDEM-X DEM and InSAR Analyses. Rem. Sens. 14 (3), 637. https://doi.org/10.3390/rs14030637.

Timmerman, A., Haasnoot, M., Middelkoop, H., Bouma, T., McEvoy, S., 2021. Ecological consequences of sea level rise and flood protection strategies in shallow coastal systems: a quick-scan barcoding approach. Ocean Coast Manag. 210, 105674 https://doi.org/10.1016/j.ocecoaman.2021.105674.

Wahl, T., Jain, S., Bender, J., Meyers, S.D., Luther, M.E., 2015. Increasing risk of compound flooding from storm surge and rainfall for major US cities. Nat. Clim. Change 5 (12), 1093–1097. https://doi.org/10.1038/nclimate2736.

Wang, J., Gao, W., Xu, S., Yu, L., 2012. Evaluation of the combined risk of sea level rise, land subsidence, and storm surges on the coastal areas of Shanghai, China. Climatic Change 115 (3–4), 537–558. https://doi.org/10.1007/s10584-012-0468-7.

Wang, J., Yi, S., Li, M., Wang, L., Song, C., 2018. Effects of sea level rise, land subsidence, bathymetric change and typhoon tracks on storm flooding in the coastal areas of Shanghai. Sci. Total Environ. 621, 228–234. https://doi.org/10.1016/j.scitotenv.2017.11.224.

Wang, Y., Marsooli, R., 2021. Dynamic modeling of sea-level rise impact on coastal flood hazard and vulnerability in New York City's built environment. Coastal Engineering 169, 103980. https://doi.org/10.1016/j.coastaleng.2021.103980.

Xu, H., Ragno, E., Tan, J., Antonini, A., Bricker, J.D., Jonkman, S.N., Liu, Q., Wang, J., 2023. Perspectives on compound flooding in Chinese estuary regions. International Journal of Disaster Risk Science 14 (2), 269–279. https://doi.org/10.1007/s13753-023-00482-1.

Xu, H., Xu, K., Lian, J., Ma, C., 2019. Compound effects of rainfall and storm tides on coastal flooding risk. Stoch. Environ. Res. Risk Assess. 33 (7), 1249–1261. https://doi.org/10.1007/s00477-019-01695-x.

Xu, H., Zhang, X., Guan, X., Wang, T., Ma, C., Yan, D., 2022. Amplification of flood risks by the compound effects of precipitation and storm tides under the Nonstationary scenario in the coastal city of Haikou, China. International Journal of Disaster Risk Science 13 (4), 602–620. https://doi.org/10.1007/s13753-022-00429-y.

Yin, J., Jonkman, S., Lin, N., Yu, D., Aerts, J., Wilby, R., Pan, M., Wood, E., Bricker, J., Ke, Q., Zeng, Z., Zhao, Q., Ge, J., Wang, J., 2020. Flood risks in Sinking Delta cities: time for a Reevaluation? Earth's Future 8 (8), e2020EF001614. https://doi.org/10.1029/2020EF001614.

Yuan, Y., Jia, L.Y., Zhang, L.J., Liu, J.C., Zhu, H.Y., 2020. Land subsidence monitoring and mechanism analysis in Haikou based on SBAS-InSAR technology. Geogr. Geo-Inf. Sci. 36 (5), 56–64. https://doi.org/10.3969/j.issn.1672-0504.2020.05.008 in Chinese.

Zeng, P., Su, Z.H., Fang, W.H., Zhang, H.X., Yu, L., 2022. Typhoon flooding loss assessment in Haikou city based on high precision building Type data. Journal of Catastrophology 37 (4), 155–165. https://doi.org/10.3969/j.issn.1000-811X.2022.04.025 in Chinese.

Zhao, L., Liu, F., 2020. Land-use planning adaptation in response to SLR based on a vulnerability analysis. Ocean Coast Manag. 196, 105297 https://doi.org/10.1016/j.ocecoaman.2020.105297.

Zhao, Q., Pan, J., Devlin, A., Xu, Q., Tang, M., Li, Z., Zamparelli, V., Falabella, F., Mastro, P., Pepe, A., 2021. Integrated analysis of the combined risk of ground subsidence, Sea Level rise, and natural hazards in coastal and Delta river regions. Rem. Sens. 13 (17), 3431. https://doi.org/10.3390/rs13173431.